Proceedings of the ASME 2015 34th International Conference on
Ocean, Offshore and Arctic Engineering
OMAE 2015
May 31 – June 5, 2015, St. John's, NL, Canada

OMAE2015-41674

DRAFT: HIGH-FIDELITY FLUID STRUCTURE COUPLED SIMULATIONS FOR UNDERWATER PROPULSION USING FLEXIBLE BIOMIMETIC FINS

Howard J. Chung
Department of Aerospace and
Ocean Engineering
Virginia Polytechnic Institute and
State University
Blacksburg, Virginia 24061

Ashok K. Kancharala
Department of Aerospace and
Ocean Engineering
Virginia Polytechnic Institute and
State University
Blacksburg, Virginia 24061

Michael K. Philen
Department of Aerospace and
Ocean Engineering
Virginia Polytechnic Institute and
State University
Blacksburg, Virginia 24061

Kevin G. Wang*
Department of Aerospace and
Ocean Engineering
Virginia Polytechnic Institute and
State University
Blacksburg, Virginia 24061

ABSTRACT

The ability of fish to maneuver in tight places, perform stable high acceleration maneuvers, and hover efficiently has inspired the development of underwater robots propelled by flexible fins mimicking those of fish. In general, fin propulsion is a challenging fluid-structure interaction (FSI) problem characterized by large structural deformation and strong added-mass effect. It was recently reported that a simplified computational model using the vortex panel method for the fluid flow is not able to accurately predict thrust generation. In this work, a high-fidelity, fluid-structure coupled computational framework is applied to predict the propulsive performance of a series of biomimetic fins of various dimensions, shapes, and stiffness. This computational framework couples a three-dimensional finite-volume Navier-Stokes computational fluid dynamics (CFD) solver and a nonlinear, finite-element computational structural dynamics (CSD) solver in a partitioned procedure. The large motion and deformation of the fluid-structure interface is handled using a validated, state-of-the-art embedded boundary method. The notorious numerical added-mass effect, that is, a numerical instability issue commonly encountered in FSI simulations involving incompressible fluid flows and light (compared to fluid) structures, is suppressed by accounting for water compressibility in the CFD model and applying a low-Mach preconditioner in the CFD solver. Both one-way and two-way coupled simulations are performed for a series of flexible fins with different thickness. Satisfactory agreement between the simulation prediction and the corresponding experimental data is achieved.

INTRODUCTION

The high maneuverability and adaptability of fish to various swimming requirements have inspired the development of bio-inspired underwater robots [1-3]. The ability to modulate fin stiffness, actuate muscles, and control heaving and pitching motions are among the complex mechanical system of a fish that affects speed, maneuverability, and propulsive efficiency. Extensive efforts have been made to understand and model the

* Address all correspondence to this author.

kinematics and stiffness effects on propulsive performance using theoretical, experimental, and computational methods [4-11].

Along with fin stiffness, the stiffness of the joint connecting the fish body to the tail plays a major role in the generation of thrust. Using theoretical and experimental methods, Kancharala and Philen [11] showed that for different operating conditions, there exist a different optimal combination of fin and compliant joint stiffness for maximum efficiency. They reported that although the simplified computational model using a 2D unsteady panel method coupled with the 3D structural deformation obtained experimentally from digital image correlation (DIC) could predict the performance behavior, it was not able to accurately predict thrust magnitudes that are comparable to the experimental data.

In this work, a high-fidelity, fluid-structure coupled computational framework proposed in [14-20] is applied to simulate a series of experiments reported in [11]. The objective is twofold: (1) to verify the conclusion of [11] that the inaccurate prediction of thrust magnitude is caused by the 2D panel method; and (2) to demonstrate that the high-fidelity computational framework is capable of accurately predicting the propulsive performance of flexible biomimetic fins, therefore is a powerful tool for designing new fins. The applied computational framework couples a three-dimensional finite volume compressible Navier-Stokes CFD solver and a nonlinear, finite-element computational structural dynamics (CSD) solver in a partitioned procedure. Key components include: (1) an embedded boundary method based on local, one-dimensional multi-material Riemann solvers [15, 17]; (2) robust and efficient algorithms for tracking the fluid-structure interface with respect to the non body-fitted CFD mesh [16, 19]; (3) conservative methods for transferring the fluid-load to the finite element structural model [15, 19]; (4) a low-Mach preconditioner to efficiently solve low-speed flows near the incompressibility limit using a finite volume compressible flow solver [20]; and (5) high-order and numerically stable fluid-structure coupled time-integrators [14]. This computational framework has been successfully validated for several engineering applications including underwater implosion [18, 22], pipeline explosion [19], and the flight of flapping wing micro aerial vehicles [21].

Two types of simulations are performed to demonstrate the capability of the computational framework and validate it against the experiment. First, one-way coupled simulations are performed for a series of six fins with thickness varying from 0.2 mm to 3.2 mm, in which the motion and deformation of the structure (i.e. joint-fin system) is prescribed by the piecewise linear interpolation of DIC images obtained from the experiments that are simulated. Next, a finite element model of the structure is constructed using shell elements, and two-way coupled simulations are performed. The results from the two-way coupled simulations are indeed *predictions*, as no experimental result is provided to the simulation, and the only empirical inputs are the material properties of the involved fluid and solid.

The remainder of this paper is organized as follows: The second section, Computational Framework, describes the mathematical models and computational methods for the fluid flow, the structure, and their interaction. The third section, Application, presents two series of simulations using the aforementioned computational framework and the comparison between simulation and experimental results.

COMPUTATIONAL FRAMEWORK

In general, fin propulsion is a challenging fluid-structure interaction (FSI) problem characterized by highly nonlinear hydrodynamics and large structural deformation. Due to the large fluid-solid density ratio (~1) and the small thickness of the fins (10^{-1}~10^{1} mm), it also exhibit strong added mass effect, which poses a significant numerical challenge to fluid-structure coupling, especially when the fluid is assumed incompressible [23, 24]. In this work, we model water as a compressible Newtonian fluid, governed by the three-dimensional Navier-Stokes equation. The structure is modeled as a thin shell, and the fluid-structure interface is assumed to be impermeable.

Computational Fluid Dynamics (CFD)

Equations of State Water is modeled in this work as a compressible fluid. Therefore an equation of state (EOS) is required to close the governing Navier-Stokes equations. Specifically, Tait's barotropic EOS in the form of:

$$p = p_0 + \alpha\left(\left(\frac{\rho}{\rho_o}\right)^{\beta} - 1\right) \tag{1}$$

is used, where

$$\alpha = p_0 + \frac{k_1}{k_2}, \beta = k_2 \tag{2}$$

k_1, k_2, ρ_0, p_0 are empirical coefficients. For water and the SI units, these two constants are experimentally determined to be $k_1 = 2.07E9,\ k_2 = 7.15, p_0 = 1.0E5\ Pa,\ \rho_0 = 1.0E3\ kg/m^3$

Governing Equations of Dynamic Equilibrium Let $\Omega_F \subset \Re^3$ denote the fluid domain of interest. The governing Navier-Stokes equations can be written in vector and conservation form as:

$$\begin{aligned}
&\frac{\partial \rho}{\partial t} + \frac{\partial(\rho u)}{\partial x} + \frac{\partial(\rho v)}{\partial y} + \frac{\partial(\rho w)}{\partial z} = 0 \\
&\rho\left(\frac{\partial u}{\partial t} + u\frac{\partial u}{\partial x} + v\frac{\partial u}{\partial y} + w\frac{\partial u}{\partial z}\right) = -\frac{\partial p}{\partial x} + \mu\left(\frac{\partial^2 u}{\partial x^2} + \frac{\partial^2 u}{\partial y^2} + \frac{\partial^2 u}{\partial z^2}\right) \\
&\rho\left(\frac{\partial v}{\partial t} + u\frac{\partial v}{\partial x} + v\frac{\partial v}{\partial y} + w\frac{\partial v}{\partial z}\right) = -\frac{\partial p}{\partial y} + \mu\left(\frac{\partial^2 v}{\partial x^2} + \frac{\partial^2 v}{\partial y^2} + \frac{\partial^2 v}{\partial z^2}\right) \\
&\rho\left(\frac{\partial w}{\partial t} + u\frac{\partial w}{\partial x} + v\frac{\partial w}{\partial y} + w\frac{\partial w}{\partial z}\right) = -\frac{\partial p}{\partial z} + \mu\left(\frac{\partial^2 u}{\partial x^2} + \frac{\partial^2 u}{\partial y^2} + \frac{\partial^2 u}{\partial z^2}\right)
\end{aligned} \tag{3}$$

where *t* denotes time, ρ the fluid density, u, v, w the orthogonal components of fluid velocity in the orthogonal direction x, y, z, p the fluid pressure, $\mu = 1.0 \times 10^{-3}\, Pa \cdot s$ the dynamic viscosity of liquid water at 20°*C*.

Non Body-Fitted Semi-Discretization The large structural motions and deformations that characterize fin propulsion challenge the efficiency, if not robustness, of the mesh motion schemes needed for implementing an Arbitrary Lagrangian-Eulerian (ALE) computational framework for fluid-structure interaction. For this reason, the governing fluid Eq. (3) is kept here in its Eulerian setting and semi-discretized by a finite volume method on a *non body-fitted* grid. This allows handling large structural motions and deformations, contact, and even topological change, in a robust manner. The basic steps of the semi-discretization are outlined below.

Let D_h denote a non body-fitted discretization of the fluid domain of interest Ω_F, where the subscript h designates the maximal length of the edges of this discretization. For every vertex $V_i \in D_h$, a cell or control volume C_i is constructed (see Figure 1 for an illustration in 2D).

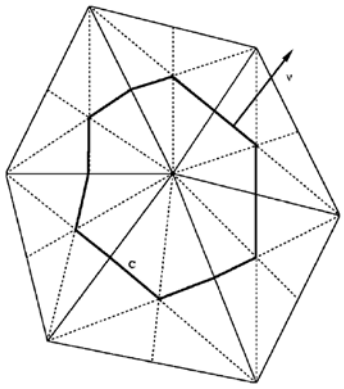

FIGURE 1: Control volume or cell *C* for a finite volume method (two-dimensional case)

For example if D_h consists of tetrahedral, C_i is defined as the union of the volumes resulting from subdividing each tetrahedron D_h having V_i as a vertex by the quadrangular surfaces containing a mid-point of an edge of the tetrahedron, the centroid of this tetrahedron, and two of the face centroids. The boundary surface of C_i is denoted here by, ∂C_i and the unit outward normal to ∂C_i is denoted by $\boldsymbol{n_i} = \left(n_{i_x}, n_{i_y}, n_{i_z}\right)^T$. The union of all of the control volumes defines a dual discretization of D_h. Using the standard characteristic function associated with a control volume C_i, a standard variational approach, and integration by parts, Eq. (3) can be transformed into its weaker form:

$$\int_{C_i} \frac{\partial \boldsymbol{W}_h}{\partial t} d\Omega + \sum_{j \in K(i)} \int_{\partial C_{ij}} \boldsymbol{F}(\boldsymbol{W}_h) \cdot \boldsymbol{n}_{ij} d\Sigma + \int_{\partial C_i \cap \Sigma_E} \boldsymbol{F}(\boldsymbol{W}_h) \cdot \boldsymbol{n}_E d\Sigma + \int_{\partial C_i \cap \Sigma_\infty} \boldsymbol{F}(\boldsymbol{W}_h) \cdot \boldsymbol{n}_\infty d\Sigma = 0 \quad (4)$$

where $\boldsymbol{W}_h$ denotes the semi-discrete state vector, $K(i)$ denotes the set of neighboring vertices of V_i, $\partial C_{ij} \equiv \partial C_i \cap \partial C_j$, $\boldsymbol{n}_{ij}$ is the unit outward normal to ∂C_{ij}, Σ_E is the discrete approximation of the wet surface of the structure – and therefore the fluid-structure interface – that is embedded in D_h, $\boldsymbol{n}_E$ is the unit outward normal to Σ_E, Σ_∞ denotes the far-field boundary of the flow, and $\boldsymbol{n}_\infty$ is its unit outward normal. This weaker form reveals that in practice, the flow computations are performed in a one-dimensional manner, essentially by evaluating fluxes along normal directions to boundaries of the control volumes. For this purpose, ∂C_i is split in the control volume boundary facets ∂C_{ij} connecting the centroids of the tetrahedra having V_i and V_j as common vertices. Then, fluxes in the interior of fluid domain is approximated by:

$$\sum_{j \in K(i)} \int_{\partial C_{ij}} \boldsymbol{F}(\boldsymbol{W}_h) \cdot \boldsymbol{n}_{ij} d\Sigma \approx \sum_{j \in K(i)} \Phi_{Roe}(W_i, W_j, \text{EOS}, \boldsymbol{n}_{ij}), \quad (5)$$

Where Φ_{Roe} is a numerical flux function associated with the second-order extension of the Roe flux based on the MUSCL (Monotonic Upwind Scheme Conservation Law), and W_i and W_j denote the average values of $\boldsymbol{W}_h$ in cells C_i and C_j, respectively. The last two terms in (4) correspond to the fluxes across the fluid-structure interface and at the far field boundary, respectively. The computation of the fluxes across the fluid-structure interface is discussed in the Section *Fluid-Structure Interaction with Large Structural Deformations*.

Low-Mach Preconditioner In order to restore the correct asymptotic behavior of the pressure when the Mach number goes to zero in the regions of low-speed flow, the Roe flux is also equipped with local preconditioning [17].

Finally, the ordinary differential equation resulting from the semi-discretization can be expressed in a compact form as:

$$\frac{d\mathbf{W}}{dt} + \mathbf{F}(\mathbf{W}) = 0 \quad (6)$$

where $\boldsymbol{W}$ and $\boldsymbol{F}$ denote the cell-averaged state vector and the numerical flux function for the entire mesh.

Computational Structural Dynamics (CSD)

Governing Equations of Motion The Lagrangian equations of motion of the nonlinear flexible structure Ω_S can be written in a compact form:

$$\rho_S \frac{\partial^2 u_j}{\partial t^2} = \frac{\partial}{\partial x_i}\left(\sigma_{ij} + \sigma_{im}\frac{\partial u_j}{\partial x_m}\right) + b_j \quad \text{in } \Omega_S, \quad j = 1,2,3 \qquad (7)$$

where the subscripts designate the coordinate system (x, y, z), $\boldsymbol{u}$ is the displacement vector field of the structure, $\boldsymbol{\sigma}$ is the second Piola-Kirchhoff stress tensor, and $\boldsymbol{b}$ the vector of body forces acting in Ω_S.

Semi-Discretization The nonlinear structural equations of motion (7) are typically semi-discretized by the Lagrangian finite element (FE) method. This leads to the discrete equations

$$\mathbf{M}\frac{\partial^2 \mathbf{u}}{\partial t^2} + \mathbf{f}^{int}(\mathbf{u}, \frac{\partial \mathbf{u}}{\partial t}) = \mathbf{f}^{F}(\mathbf{w}) + \mathbf{f}^{ext}, \qquad (8)$$

where $\mathbf{M}$ denotes the symmetric positive definite mass matrix, $\mathbf{u}$ denotes the vector of discrete structural displacements, and $\mathbf{f}^{int}$, $\mathbf{f}^{ext}$, $\mathbf{f}^{F}$ denote the vectors of internal, external, and flow-induced discrete forces, respectively.

Fluid-Structure Interaction (FSI) using Embedded Boundary Method

Transmission Conditions Assuming an impermeable interface, the interaction between the fluid and structure subsystems represented by Eq. (3) and Eq. (7), respectively, is driven by two transmission conditions: the kinematic, non-penetration condition

$$\left(\boldsymbol{v} - \frac{\partial \boldsymbol{u}}{\partial t}\right) = 0 \quad \text{on } \Sigma_w \qquad (9)$$

and the equilibrium condition

$$\left(\sigma_{ij} + \sigma_{im}\frac{\partial u_j}{\partial x_m} + P\delta_{ij}\right)n_{w_i} - T_j = 0 \quad \text{on } \Sigma_w \qquad (10)$$

where Σ_w denotes the physical fluid-structure interface whose FE discretization is Σ_E, $\boldsymbol{n}_w$ is the unit outward normal to Σ_w, and T_j denotes the tractions due to external forces whose origin is not due to the flow.

Embedded Boundary Method for FSI The interface transmission conditions Eq. (9) and Eq. (10) are semi-discretized using the embedded boundary method for CFD ([15]). More specifically, the embedded discrete fluid-structure interface Σ_E is represented within D_h by the surrogate interface $\tilde{\Sigma}_E$ defined in Eqn. (11) (See Figure 2 for illustration), and constructed using either interface tracking algorithm described in [16].

$$\tilde{\Sigma}_E = \bigcup_{(i,j)/V_iV_j \cap \Sigma_E \neq \emptyset} \partial C_{ij} \qquad (11)$$

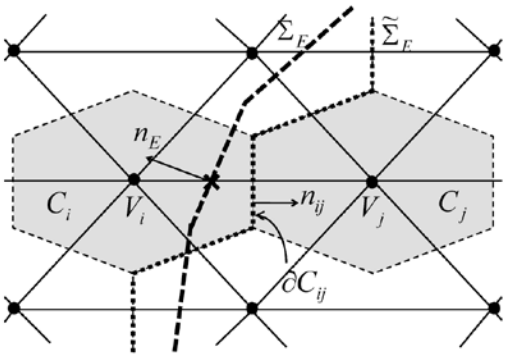

FIGURE 2: Two-dimensional illustration of the embedded boundary method

Then, the interface condition Eqn. (9) is enforced in two steps as follows:

(i) For each edge V_iV_j of the fluid mesh that intersects the embedded discrete interface Σ_E that is, for each $V_iV_j \cap \Sigma_E \neq \emptyset$, a one-dimensional fluid-structure Riemann problem between each vertex of this edge (V_i or V_j) and Σ_E, is constructed and solved using the structure velocity at the intersection point.

(ii) For each edge V_iV_j of the fluid mesh that intersects the embedded discrete interface Σ_E, a contribution to the third term in Eq. (4) is evaluated by computing the numerical flux on each side of the fluid-structure interface as follows:

$$\int_{\partial C_i \cap \Sigma_E} \boldsymbol{F}(\boldsymbol{W}_h)\cdot \boldsymbol{n}_E d\Sigma \approx \int_{\partial C_i \cap \tilde{\Sigma}_E} \boldsymbol{F}(\boldsymbol{W}_h)\cdot \boldsymbol{n}_{ij} d\Sigma$$
$$= \int_{\partial C_{ij}} \boldsymbol{F}(W_h^{(i)})\cdot \boldsymbol{n}_{ij} d\Sigma \approx \Phi_{Roe}(W_i, W_M^{(i)}, \mathrm{EOS}^{(i)}, \boldsymbol{n}_{ij}) \qquad (12)$$

and

$$\int_{\partial C_j \cap \Sigma_E} \boldsymbol{F}(\boldsymbol{W}_h)\cdot \boldsymbol{n}_E d\Sigma \approx \int_{\partial C_j \cap \tilde{\Sigma}_E} \boldsymbol{F}(W_h)\cdot \boldsymbol{n}_{ji} d\Sigma$$
$$= \int_{\partial C_{ij}} \boldsymbol{F}(W_h^{(j)})\cdot \boldsymbol{n}_{ji} d\Sigma$$
$$\approx \Phi_{Roe}(W_j, W_M^{(j)}, \mathrm{EOS}^{(j)}, \boldsymbol{n}_{ji}), \qquad (13)$$

Where $W_M^{(i)}$ $\left(W_M^{(j)}\right)$ is the solution of the one-dimensional fluid-structure Riemann problem between $V_i\left(V_j\right)$ and Σ_E. It is notable that the velocity components of $W_M^{(i)}$ and $W_M^{(j)}$ verify the interface transmission condition Eqn. (9).

As for the interface transmission condition Eqn. (10), it is enforced using the conservative load transfer algorithm proposed in [15]. Briefly, this algorithm can be summarized as follows:

(i) Transform the pressure components of $W_M^{(i)}$ and $W_M^{(j)}$ into local force loads $\mathbf{f}^F\left(P_M^{(i)}\right)$ and $\mathbf{f}^F\left(P_M^{(j)}\right)$

(ii) Distribute these loads onto the wetted surface of the FE structural model as external forces.

Fluid-Structure Coupled Time-Integrator: The 2nd-order accurate time-integrator presented in [14] is applied in this work to integrate the fluid and structure subsystems in a partitioned procedure (Fig. 3).

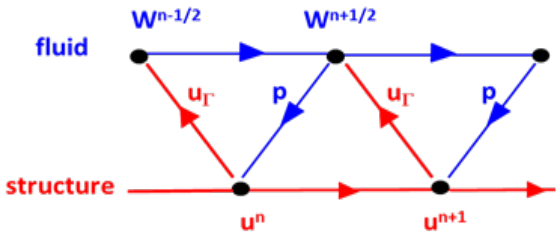

FIGURE 3: A staggered, 2nd-order and provably stable time-integrator for fluid-structure coupled systems [14].

APPLICATION

The combined effect of fin and joint flexibility on propulsive performance was studied in [11] through a series of experiments. The joint stiffness was kept constant, while the fin effective flexural stiffness was varied by varying the fin thickness. Fin test coupons of different fin thickness (different effective flexural stiffness) were fabricated and tested in low speed (0.1 to 1 m/s) flow.

The Reynolds number

$$Re = \frac{\rho_\infty V_\infty c}{\mu} \tag{14}$$

is used to characterize the fluid flow, while the Strouhal number

$$St_h = \frac{2h_o f}{V_\infty} \tag{15}$$

is used to characterize frequency and heaving amplitude at a given Reynolds number. Here ρ_∞ is the free stream water density, V_∞ is the free stream velocity, c is the characteristic length represented by the total chord of the joint and fin, μ is the dynamic viscosity of water at room temperature, and $2h_o$ is the heaving amplitude. For the experiments reported in [11], the Reynolds number is of the order of 10^3-10^4 whereas the Strouhal number is around 0.2.

The digital image correlation (DIC) technique was employed in the experiment to capture the time-history of the motion and deformation of the structure. This data, as shown in [11], can be used as input in a fluid-structure coupled analysis, leading to one-way coupled simulations.

In this work, we first couple the structural motion and deformation obtained from DIC with the 3D Navier-Stokes CFD solver to test the fluid subsystem of the computational framework. Then, a finite element model is constructed to represent the structure, which is then used in a two way coupled CFD – CSD simulation. The quantitative propulsive thrust results from the four approaches will be compared: (1) Experiment [11]; (2) Vortex Panel – DIC Coupled Simulation [11]; (3) One-way CFD – DIC Coupled Simulation; and (4) Two-way CFD – CSD Coupled Simulation.

TABLE 1: The different approaches considered in this work to study the propulsive performance of flexible biomimetic fins

Approach	Key Features
Experimental [11]	• Provided baseline for comparison • Instrumentation require significant time and resource • Low fidelity data acquisition and environmental uncertainty, "noise" require validation
Vortex Panel – DIC coupled simulation [11]	• Low fidelity 2D unsteady discrete vortex panel • 2D thin lifting airfoil modeled from centerline of 3D DIC fin deformation • Inviscid, incompressible fluid
One way coupled CFD – DIC simulation	• Structural motion deformation is prescribed • Compressible viscous fluid flow
Two way coupled CFD – CSD simulation	• High fidelity two way coupled simulation • Compressible viscous fluid flow • Thin shell structure

Experiment The combined effect of fin and joint stiffness on propulsive performance has been studied by testing artificial fins in a water tunnel. The experimental setup is shown in Figure 4. The trapezoidal artificial fins have been fabricated using Polycarbonate (PC) sheets having the same span, chord, but different thickness values ranging from 0.2 to 3.2 mm. To mimic the joint, a rectangular PC sheet of 0.4 mm thickness is attached to the fins using an Aluminum plate. The dimensions of the fin and joint configuration are shown in Figure 5.

A 6" × 6" × 18" recirculating water tunnel is used for the experiment, and a constant free stream velocity of 0.1 m/s is maintained throughout the experiment. The flapping mechanism houses two CUI M223X0003 brushed dc motors attached with encoders which provides pitching and heaving motion. The

frequency and phase difference between the two motors can be controlled independently of each other. Although combined pitching and heaving motion describe the kinematics of fish fins, in this study, only the heaving motion is considered. The fins are operated at a frequency of 1 Hz with a heaving amplitude of 20 mm.

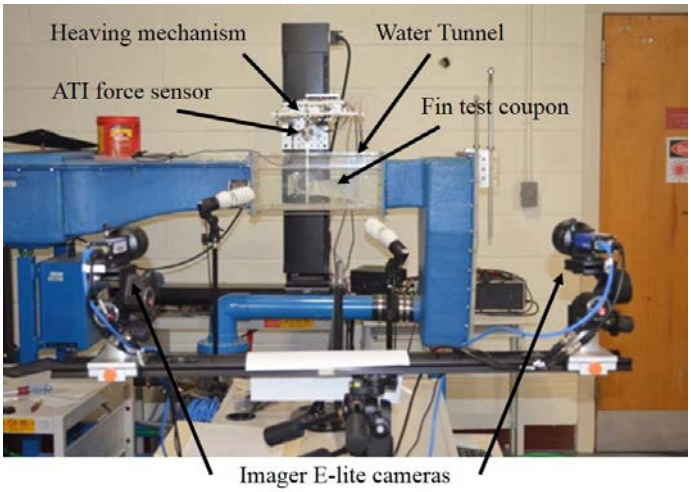

FIGURE 4: Experimental setup for evaluating flexible fins in a water tunnel

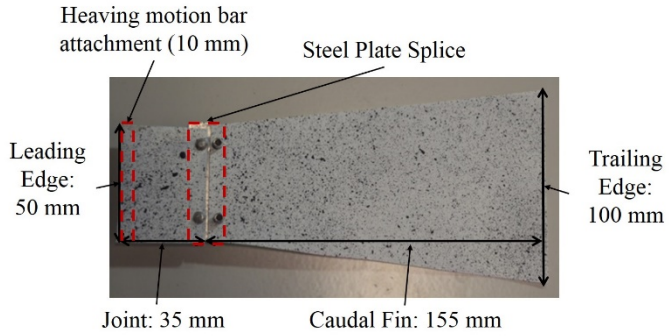

FIGURE 5: Speckled fin and joint test coupon used for DIC data acquisition

A six axis force transducer, ATI MINI40, is used to measure the forces and moments acting on the flapping foils, where one end of the transducer is connected to the rod linked to the scotch-yoke mechanism and the other end is connected to the bar which mounts the flapping foil.

To obtain the time-averaged thrust values, 3 runs for each fin-joint combination were conducted. 10 – 20 cycles for each run were obtained and its mean thrust values were calculated. The difference between the three mean thrust values for each test case were low. For example, for the 3.2 mm fin thickness, the three mean thrust values are 0.0058 N, 0.0052 N, and 0.0055 N. The average value values are shown in Table 2.

Along with measuring the forces acting on the flapping fins, the deformation of the fins is captured using digital image correlation (DIC). DIC is a technique that uses digital imaging processing methods to track the speckled pattern on the surface of the fin (Figure 5). The setup consists of two Imager E-lite cameras mounted on a single tripod with a horizontal slider bar, two fluorescent lights, and a LaVision Programmable Timing Unit computer with DaVis 8.1 software. The cameras are capable of capturing the images at a frequency of 14 Hz. Calibration was performed using a custom-made calibration plate which covers the entire range of expected deformation. A third order polynomial fitting function was used for calibration since the fins were tested underwater, causing diffraction. A detailed description of the experimental setup can be found in [11].

Vortex Panel - DIC Coupled Simulation A series of simulations are presented in [11] in which the fluid flow is modeled using a 2D vortex panel method. The piecewise linear interpolation of the DIC data is used to prescribe the time-history of the structural motion and deformation. The predicted thrust is found to be significantly higher than the corresponding experimental measurement (Table 2). For example, for a fin of 0.4 mm thickness the discrepancy is around 1200%.

One-Way Coupled CFD-DIC Simulation As a validation of the fluid subsystem of the computational framework, a series of one-way coupled simulations are first performed. In these simulations, the piecewise linear interpolation of the DIC data is again used to prescribe the time-history of the motion and deformation of the structure. The three-dimensional compressible Navier-Stokes equations (1) are solved. The boundary conditions were setup to mimic the boundary conditions in the experimental procedure (Figure 6). The fluid mesh contains 1.5M nodes, 9M tetrahedrons and the simulations were performed on 320 processor cores. Local refinement of the tetrahedron mesh is performed in the area that the embedded fin traverses.

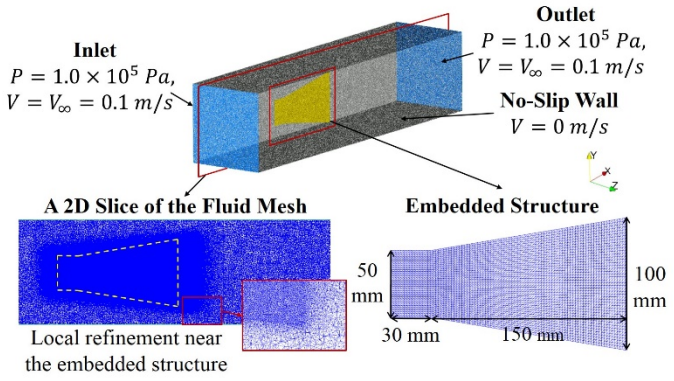

FIGURE 6: One way Coupled CFD – DIC Simulation

The main objective of these simulations is to validate the finite volume CFD solver and the embedded boundary method for fluid-structure interaction. It should be noted that the solution of interest here is the fluid response to the dynamic embedded surface. Figures 7 and 8 show the instantaneous hydrodynamic pressure field and the velocity field. The capability of the computational framework to capture the transient, highly nonlinear flow behavior is clearly evident. The 2D cut of velocity magnitude in the x-z plane from Figure 8 is capable of giving insight on the development of vortices from the root of the fin to the trailing wake region of the oscillating fin. It is noted that the velocity (magnitude) field surrounding the fin with 0.4 mm thickness is higher than that of 1.6 mm. This implies a larger "lift" force acting on more flexible fins. Also, the capability to post-process the fluid flow in either the x-z plane, x-y plane or 3D solution allows users to study the development of vortex cores, alternating vortex pairs, as well as their interaction with each other. This is a significant piece of information for bio-inspired researchers that is difficult to be accomplished via experimental techniques.

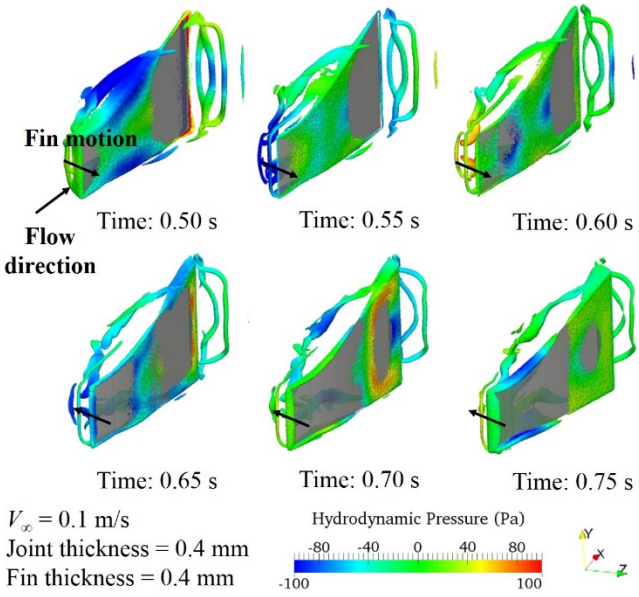

FIGURE 7: 3D visualization of vorticity contour (colored by pressure)

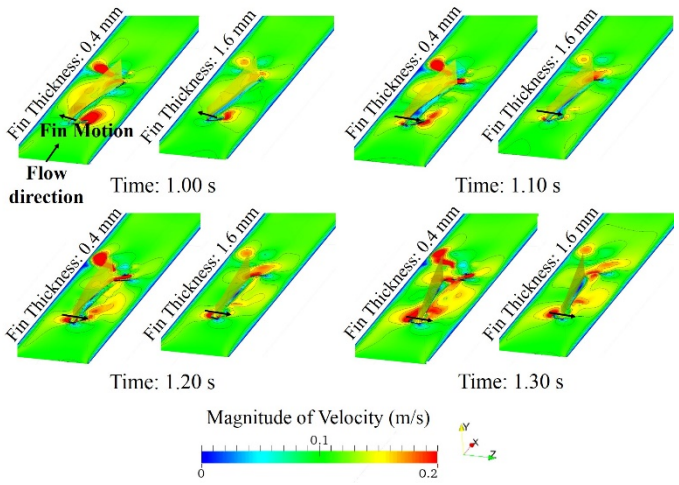

FIGURE 8: 2D cut view of velocity magnitude for 0.4 mm and 1.6 mm fin thickness in one way CFD – DIC simulation

The pressure and viscous forces are integrated along the surface of the fin to obtain the thrust in the negative x direction. The quantitative results are tabulated in Table 2. The thrust values predicted by the CFD-DIC simulations are significantly closer to the corresponding experimental measurement, compared to the vortex panel based simulations reported in [11].

TABLE 2: Time –averaged thrust of various fin thickness obtained from experiment, vortex panel – DIC coupled simulation, and CFD – DIC coupled simulation

Fin Thickness (mm)	Time – Averaged Thrust (N)		
	Experimental	Vortex Panel – DIC	CFD – DIC Simulation
0.2	0.0335	0.3880	0.0440
0.4	0.0138	0.1868	0.0210
0.7	0.0023	0.1836	0.0021
1.2	-0.0153	0.1428	0.0009
1.6	-0.0127	0.1388	-0.0013
3.2	-0.0055	0.1425	-0.0008

Two-Way Coupled CFD-CSD Simulation To fully validate the fluid-structure coupled computational framework, a finite element structural model is constructed (Figure 9). It contains 1314 nodes and 2460 quadrangle thin shell elements. Effort was made to create as close similitude to the fin test coupons used in the experiment. This includes prescribing the sinusoidal heaving motion on nodes 1 to 66, which are located within 10 mm of the root of the fin that was connected to the bar for actuation. The splice that connected the joint and fin in the experiment was represented by a steel plate of thickness 0.4 mm and a width of 15 mm. Note that in this section, the mesh is course compared to the joint and fin. Since this is a "rigid" link,

its deformation is of less interest to the authors than is the deformation of the joint and fin.

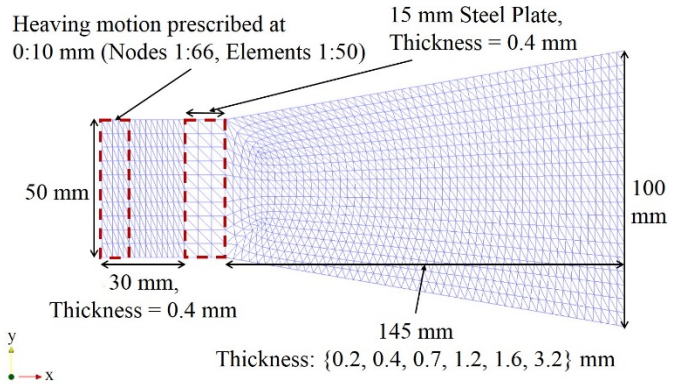

FIGURE 9: Structural model used for two way coupled CFD – CSD simulation

A "dry" (i.e. structure-only) simulation is first performed for the fin of 0.4 mm thickness to verify the finite element structural model. The heaving motion applied in the experiment is prescribed. Six snapshots of the structural deformation are shown in Figure 10, in contrast with the result obtained from the two-way coupled simulation.

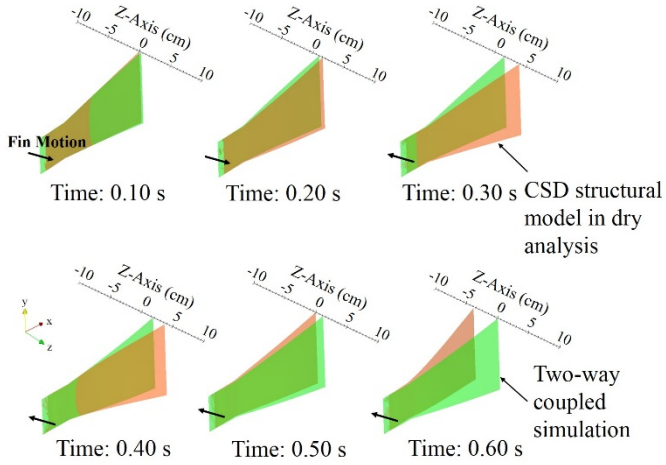

FIGURE 10: Comparison of instantaneous structural deformation of structural model in "dry" analysis and in two way coupled simulation

A two-way coupled simulation is performed for the fin of 0.4 mm thickness. Six snapshots of the fluid velocity field are shown in Figure 11, for a 2D slilce of the fluid computational domain. Again, it is shown that the computational framework is capable of capturing the highly nonlinear fluid dynamics caused by the large fin deformation.

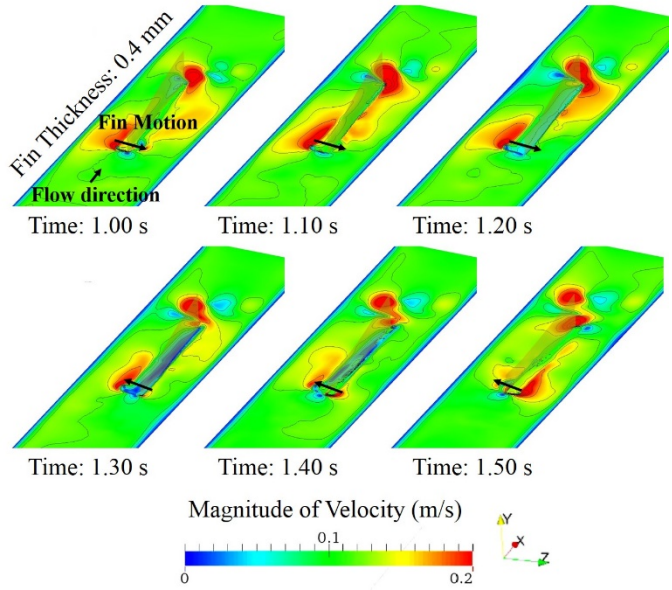

FIGURE 11: 2D cut view of velocity magnitude for 0.4 mm fin thickness in two way CFD – DIC simulation

The predicted time-averaged thrust obtained from the two-way coupled simulation is shown in Figure 12. It is 31% smaller than the corresponding experimental result. This is a significant improvement compared to the vortex panel – DIC coupled simulations, which generated 1200% error for the same fin.

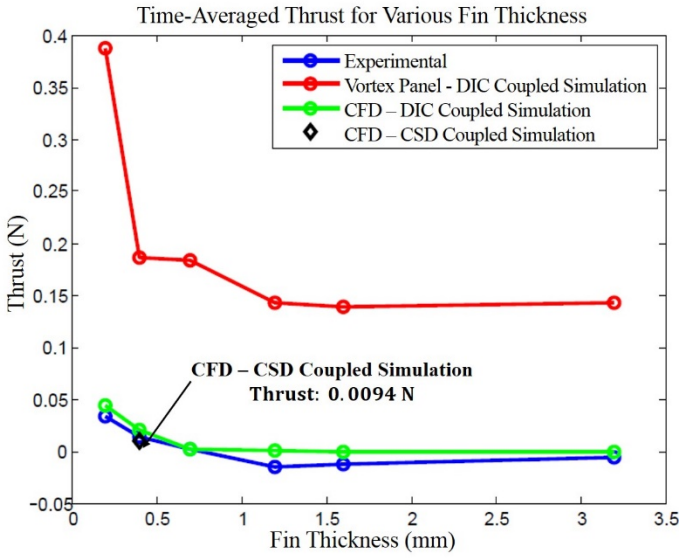

FIGURE 12: Time-averaged thrust for various fin thickness

CONCLUSION

A computational framework that couples a three dimensional finite-volume Navier-Stokes computational fluid dynamics (CFD) solver and a nonlinear, finite-element

computational structural dynamics solver is validated for underwater fin propulsion. Satisfatory agreement is obtained between the simulation prediction and the corresponding experimental measurement. In particular, for a thin, flexible fin of 0.4 mm thickness, the discrepancy between simulation and experimental results is 31%. This is a significant improvement compared to previous simulation work which models the fluid flow using a 2D vortex panel method. This observation also verifies the conclusion of [11] that the inaccurate prediction of thrust magnitude reported therein is caused by the insufficient fidelity of the 2D vortex panel method.

ACKNOWLEDGEMENT

This section will be completed in the final version of the manuscript.

REFERENCES

[1] D. S. Barrett, M. S. Triantafyllou, D. K. P. Yue, M. A. Grosenbaugh, and M. J. Wolfgang, "Drag reduction in fish-like locomotion," *Journal of Fluid Mechanics,* vol. 392, pp. 183-212, 1999.

[2] P. V. Alvarado and K. Youcef-Toumi, "Design of machines with compliant bodies for biomimetic locomotion in liquid environments," *Journal of Dynamic Systems, Measurement, and Control,* vol. 128, p. 3, 2006.

[3] Z. Zhang, M. Philen, and W. Neu, "A biologically inspired artificial fish using flexible matrix composite actuators: analysis and experiment," *Smart Materials and Structures,* vol. 19, p. 094017, 2010.

[4] B. E. Flammang and G. V. Lauder, "Speed-dependent intrinsic caudal fin muscle recruitment during steady swimming in bluegill sunfish, Lepomis macrochirus," *Journal of Experimental Biology,* vol. 211, pp. 587-598, February 15, 2008.

[5] B. E. Flammang and G. V. Lauder, "Caudal fin shape modulation and control during acceleration, braking and backing maneuvers in bluegill sunfish, Lepomis macrochirus," *Journal of Experimental Biology,* vol. 212, pp. 277-286, January 15, 2009 2009.

[6] C. J. Esposito, J. L. Tangorra, B. E. Flammang, and G. V. Lauder, "A robotic fish caudal fin: effects of stiffness and motor program on locomotor performance," *The Journal of Experimental Biology,* vol. 215, pp. 56-67, January 1, 2012 2012.

[7] G. V. Lauder, B. Flammang, and S. Alben, "Passive Robotic Models of Propulsion by the Bodies and Caudal Fins of Fish," *Integrative and Comparative Biology,* vol. 52, pp. 576-587, November 1, 2012 2012.

[8] S. Alben, "Optimal flexibility of a flapping appendage in an inviscid fluid," *Journal of Fluid Mechanics,* vol. 614, pp. 355-380, 2008.

[9] S. Alben, C. Witt, T. V. Baker, E. Anderson, and G. V. Lauder, "Dynamics of freely swimming flexible foils," *Physics of Fluids* vol. 24, p. 051901, 2012.

[10] A. K. Kancharala and M. K. Philen, "Enhanced hydrodynamic performance of flexible fins using macro fiber composite actuators," *Smart Materials and Structures,* vol. 23, p. 115012, 2014.

[11] A. K. Kancharala and M. K. Philen, "Study of flexible fin and compliant joint stiffness on propulsive performance: theory and experiments," *Bioinspiration & Biomimetics,* vol. 9, p. 036011, 2014.

[12] G. Pedro, A. Suleman, and N. Djilali, “Fluid-structure interaction issues in deformation based subsea propulsion systems”, *AIAA/ASME/ASCE/AHS/ASC Structures, Structural Dynamics and Materials Conference Technical Paper*, vol. 7, 2005.

[13] R. P. Clark, A. J. Smits, “Thrust production and wake structure of a batoid-inspired oscillating fin”, *Journal of Fluid Mechanics*, vol. 562, pp. 415-429, 2006

[14] C. Farhat, A. Rallu, K. Wang, and T. Belytschko, “Robust and Provably Second-Order Explicit-Explicit and Implicit-Explicit Staggered Time-Integrators for Highly Non-linear Compressible Fluid-Structure Interaction Problems,” *International Journal for Numerical Methods in Engineering* 2010; **84**:73-107.

[15] K. Wang, A. Rallu, J-F. Gerbeau, and C. Farhat, “Algorithms for Interface Treatment and Load Computation in Embedded Boundary Methods for Fluid and Fluid-Structure Interaction Problems,” *International Journal for Numerical Methods in Fluids*. 2011; **67**:1175-1206.

[16] K. Wang, J. Gretarsson, A. Main, and C. Farhat, “Computational Algorithms for Tracking Dynamic Fluid-Structure Interfaces in Embedded Boundary Methods,” *International Journal for Numerical Methods in Fluids*. 2012; **70**:515-535.

[17] C. Farhat, J.-F. Gerbeau and A. Rallu, "FIVER: A Finite Volume Method Based on Exact Two-Phase Riemann Problems and Sparse Grids for Multi-Material Flows with Large Density Jumps", *Journal of Computational Physics*, Vol. 231, pp. 6360-6379 (2012).

[18] K. Wang, P. Lea, A. Main, O. McGarity, and C. Farhat, “Predictive Simulation of Underwater Implosion: Coupling Multi-Material Compressible Fluids with Cracking Structures”. *Proceedings of the ASME 2014 33rd International Conference on Ocean, Offshore and Arctic Engineering (OMAE 2014).* San Francisco, California, June 2014.

[19] K. Wang, P. Lea, and C. Farhat, “A Computational Framework for the Simulation of High-Speed Multi-Material Fluid-Structure Interaction Problems with Dynamic Fracture,” *International Journal for Numerical Methods in Engineering*. (accepted)

[20] E. Turkel, “Preconditioned Methods for Solving the Incompressible and Low-Speed Compressible

Equations," *Journal of Computational Physics* **72**:277–298 (1987).

[21] C. Farhat and V. Lakshminarayan, "An ALE Formulation of Embedded Boundary Methods for Tracking Boundary Layers in Turbulent Fluid-Structure Interaction Problems", *Journal of Computational Physics*, Vol. 263, pp. 53-70 (2014)

[22] C. Farhat, K. Wang, A. Main, J.S. Kyriakides, K. Ravi-Chandar, L-H. Lee, and T. Belytschko, "Dynamic Implosion of Underwater Cylindrical Shells: Experiments and Computations," *International Journal of Solids and Structures*. 2013; **50**:2943-2961.

[23] P. Causin, J.-F. Gerbeau, and F. Nobile, "Added-mass Effect in the Design of Partitioned Algorithms for Fluid-Structure Problems", *Computer Methods in Applied Mechanics and Engineering*, 194:4506-4527 (2005).

[24] C. Forster, W.A. Wall, E. Ramm, "Artificial Added-Mass Instabilities in Sequential Staggered Coupling of Nonlinear Structures and Incompressible Viscous Flows", *Computer Methods in Applied Mechanics and Engineering*, 196:1278-1293 (2007).